The synaptotagmin C2B domain calcium-binding loops modulate the rate of fusion pore expansion

Mounir Bendahmane[a], Kevin P. Bohannon[a], Mazdak M. Bradberry[b], Tejeshwar C. Rao[a], Michael W. Schmidtke[a], Prabhodh S. Abbineni[a], Nara L. Chon[c], Sherleen Tran[c], Hai Lin[c], Edwin R. Chapman[b], Jefferson D. Knight[c], and Arun Anantharam[a,*]

[a]Department of Pharmacology, University of Michigan, Ann Arbor, MI 48109; [b]Department of Neuroscience, Howard Hughes Medical Institute. University of Wisconsin–Madison, Madison, WI 53705; [c]Department of Chemistry, University of Colorado Denver, Denver, CO 80217

ABSTRACT **In chromaffin cells, the kinetics of fusion pore expansion vary depending on which synaptotagmin isoform (Syt-1 or Syt-7) drives release. Our recent studies have shown that fusion pores of granules harboring Syt-1 expand more rapidly than those harboring Syt-7. Here we sought to define the structural specificity of synaptotagmin action at the fusion pore by manipulating the Ca^{2+}-binding C2B module. We generated a chimeric Syt-1 in which its C2B Ca^{2+}-binding loops had been exchanged for those of Syt-7. Fusion pores of granules harboring a Syt-1 C2B chimera with all three Ca^{2+}-binding loops of Syt-7 (Syt-1:7C2B$_{123}$) exhibited slower rates of fusion pore expansion and neuropeptide cargo release relative to WT Syt-1. After fusion, this chimera also dispersed more slowly from fusion sites than WT protein. We speculate that the Syt-1:7 C2B$_{123}$ and WT Syt-1 are likely to differ in their interactions with Ca^{2+} and membranes. Subsequent in vitro and in silico data demonstrated that the chimera exhibits a higher affinity for phospholipids than WT Syt-1. We conclude that the affinity of synaptotagmin for the plasma membrane, and the rate at which it releases the membrane, contribute in important ways to the rate of fusion pore expansion.**

Monitoring Editor
Patrick J. Brennwald
University of North Carolina

Received: Nov 2, 2017
Revised: Jan 22, 2018
Accepted: Feb 7, 2018

INTRODUCTION

Adrenomedullary chromaffin cells respond to sympathetic nervous system activation by releasing a multitude of potent hormones and neuropeptides into the bloodstream. Prior to release, these hormones and peptides are contained in dense core granules and are expelled as a result of Ca^{2+}-triggered exocytosis (Douglas, 1968; Carmichael and Winkler, 1985). During exocytosis, elevations in intracellular Ca^{2+} are sensed by members of the synaptotagmin (Syt) protein family, which, in concert with SNARE and SM (Sec1/Munc18-like) proteins, drive the fusion of granule and plasma membranes (Sudhof and Rizo, 1996; Sudhof and Rothman, 2009; Sudhof, 2013; Chapman, 2008).

Members of the Syt family share a common molecular architecture. This includes a short N-terminal lumenal region, a transmembrane domain, and two calcium binding modules (C2A and C2B) connected by a short linker. Ca^{2+} binding to Syt is coordinated by several oxygen atoms, predominantly from aspartate sidechains, in the C2 domains. For the chromaffin cell isoforms—Syt-1 and Syt-7—the number of bound Ca^{2+} ions is reported to differ. The C2A domains of Syt-1 and Syt-7 and the C2B domain of Syt-7 each bind three Ca^{2+} ions (Shao *et al.*, 1998; Xue *et al.*, 2010; Voleti *et al.*, 2017). However, the C2B domain of Syt-1 tends to bind two Ca^{2+} ions, with the third binding site occupied only at extremely high Ca^{2+} concentrations (Fernandez *et al.*, 2001; Cheng *et al.*, 2004). Functionally, the Syt-Ca^{2+} interaction promotes membrane penetration of portions of the C2A and C2B domains, and this penetration works in concert with SNARE zippering to drive the fusion pore open (Bai *et al.*, 2004a).

Despite their common architectures, Syt isoforms differ in their functional capacity as Ca^{2+} sensors for exocytosis (Zhang *et al.*, 2011; Moghadam and Jackson, 2013; Rao *et al.*, 2014, 2017). The difference

This article was published online ahead of print in MBoC in Press (http://www.molbiolcell.org/cgi/doi/10.1091/mbc.E17-11-0623) on February 14, 2018.

*Address correspondence to: Arun Anantharam (arunanan@umich.edu).

Abbreviations used: CH, Syt-1:7 C2B$_{123}$ chimera; EGTA, ethylene glycol-bis(2-aminoethyl ether)-*N*,*N*,*N*′,*N*′-tetraacetic acid; FRET, Förster resonance energy transfer; HEPES, 4-(2-hydroxyethyl)-1-piperazineethanesulfonic acid; ICN, integrated coordinated number; NPY, neuropeptide Y; PE, phosphatidylethanolamine; PS, phosphatidylserine; PSS, physiological salt solution; PTFS, persistence at the fusion site; pTIRF, polarized total internal reflection fluorescence; SM, Sec1/munc18-like; SNARE, soluble *N*-ethylmaleimide–sensitive factor activating; Syt-, synaptotagmin; TIRF, total internal reflection fluorescence; WT, wild type.

is particularly notable between Syt-1 and Syt-7 (Maximov *et al.*, 2008; Schonn *et al.*, 2008; Bacaj *et al.*, 2013). Perhaps the most important biochemical signature of Syt-7 that sets it apart from the other Syt isoforms is its high Ca^{2+} sensitivity. Syt-7 stimulation of SNARE-mediated liposome fusion occurs with a 400-fold-higher sensitivity to Ca^{2+} than with Syt-1 (Bhalla *et al.*, 2005). Furthermore, in dense-core granule exocytosis, fusion pores of granules bearing Syt-1 expand more rapidly and release neuropeptide cargos with faster kinetics than granules bearing Syt-7 (Rao *et al.*, 2014). After fusion, Syt-7-bearing granules exhibit a higher probability of undergoing "kiss-and-run" (i.e., cavicapture) than Syt-1-bearing granules. The observed differences in Syt function presumably emerge from the C2 domains, which form most of the cytoplasmic region of the protein. The degree of difference is remarkable given the high degree of sequence and structural similarity between Syt-1 and Syt-7. This suggests that subtle structural variations between isoforms in this region are sufficient to impose substantial functional differences.

Structurally, the Syt-7 C2A and C2B domains are essentially superimposable on the corresponding domains of Syt-1, with overlap observed for many of the individual amino acid side-chain orientations (Xue *et al.*, 2010; Voleti *et al.*, 2017). Notably, the Ca^{2+} affinities of the isolated Syt-1 and Syt-7 C2A domains in solution are nearly identical, even though the Syt-7 C2A domain binds liposome membranes at ~50-fold lower Ca^{2+} concentrations (Sugita *et al.*, 2002; Maximov *et al.*, 2008). This suggests that the enhanced Ca^{2+} sensitivity arises from stronger lipid binding by the Ca^{2+}-loaded state of Syt-7 relative to Syt-1 (Brandt *et al.*, 2012; Voleti *et al.*, 2017). In a comparison of C2B crystal structures, the only perceptible differences were the presence of a second short alpha helix on Syt-1 C2B that is absent from Syt-7 C2B and slight differences in the orientation of Ca^{2+} binding loops 1 and 3, though the latter may be attributable to crystal contacts (Fernandez *et al.*, 2001; Cheng *et al.*, 2004; Xue *et al.*, 2010).

The goal of this study was to illuminate how specific structural features of the cytoplasmic C2 domains of Syt-1 and Syt-7 dictate their function. In particular, we sought to test the effects on fusion pore expansion rates when Ca^{2+}-binding loops of the Syt-7 C2B domain are grafted onto the corresponding region of a protein otherwise identical to Syt-1 in adrenal chromaffin cells. We generated chimeric Syt-1 proteins in which Ca^{2+}-binding loops had been individually or collectively mutated to those of Syt-7. When overexpressed, granules bearing the chimera most closely resembling Syt-7—consisting of the Syt-1 core and all three C2B domain Ca^{2+}-binding loops of Syt-7 (Syt-1:7 $C2B_{123}$)—exhibited significantly slower rates of fusion pore expansion and neuropeptide cargo release relative to WT Syt-1. These granules could also be triggered to fuse more efficiently than those with WT Syt-1 (at levels equivalent to WT Syt-7 granules), demonstrating that the C2B domain loops are at least partially responsible for the particularly high Ca^{2+} affinity of Syt-7. After exocytosis, the Syt-1:7 $C2B_{123}$ chimera dispersed more slowly from sites of fusion than Syt-1. Simulations and experiments with purified C2AB domains suggest three molecular mechanisms that likely contribute to these effects: 1) equilibrium liposome cosedimentation measurements show that when all three Ca^{2+}-binding loops are modified, the chimeric C2AB domain has a higher intrinsic affinity for phosphatidylserine (PS) lipids than the WT Syt-1 C2AB; 2) stopped-flow fluorescence spectroscopy results show a slower dissociation rate of Syt-1:7 $C2B_{123}$ from PS membranes; and 3) molecular dynamics simulations further suggest that the Ca^{2+}-bound chimeric C2B domain might have an increased affinity for anionic phospholipids relative to the wild-type (WT) domain. The chimera contains two cationic lysine and arginine residues not found in WT Syt-1 in positions that may lead to increased membrane residence times. On the basis of these data, we conclude that the dissociation rate of the C2AB from the target membrane is an important factor contributing to the rate of fusion pore expansion. This model predicts that synaptotagmin C2AB domains with lower affinities for anionic phospholipids and faster membrane dissociation kinetics could mediate faster rates of fusion pore expansion during exocytosis.

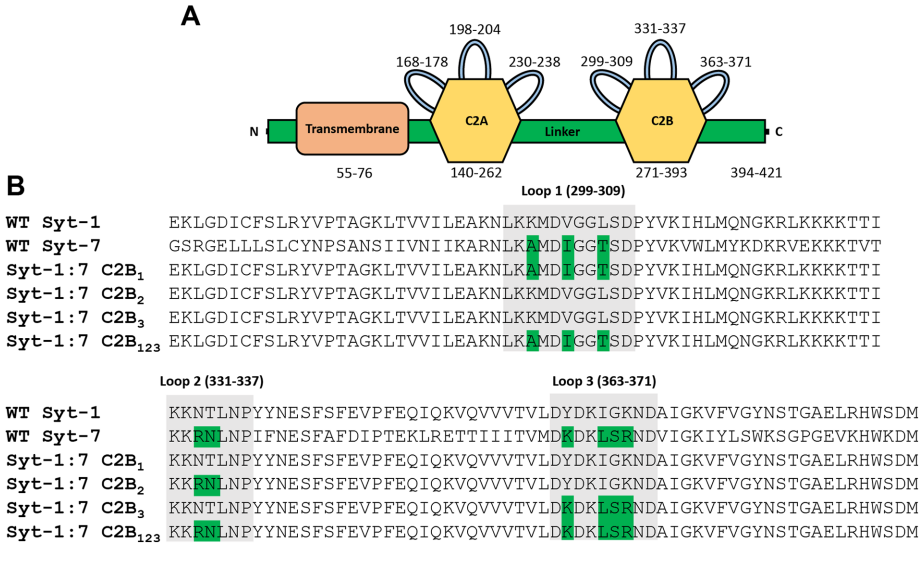

FIGURE 1: Amino acid sequences of the C2B domains from WT and chimeric Syt isoforms. (A) Simplified domain structure of synaptotagmins, showing the relative position of the transmembrane domain (red) and Ca^{2+}-binding C2A and C2B domains (yellow), each containing three Ca^{2+}-binding loops (green). A short linker connects the C2A and C2B domains (green). (B) Alignment of the C2B domain amino acid sequences of Syt-1, Syt-7, and the four chimeric Syt constructs. Amino acids highlighted in green indicate a deviation from the WT Syt-1 sequence. The gray-shaded regions denote the Ca^{2+}-binding loops. Subscript numbers in the construct name indicate which C2B loop(s) has been mutated to match WT Syt-7. Amino acid ranges based on the Syt-1 sequence are listed below each loop.

RESULTS

The Ca^{2+}-binding loops of the Syt-1 C2B modulate fusion pore dynamics

To investigate the role of the Syt-1 C2B domain Ca^{2+}-binding loops in fusion pore expansion, we generated a series of chimeric proteins (Figure 1). We started with the rat Syt-1 amino acid sequence and converted nonidentical amino acid residues of Syt-1 C2B Ca^{2+}-binding loops to match those of Syt-7 via site-directed mutagenesis (Figure 1B). In three of the chimeras, we replaced loop 1, 2, or 3 (Syt-1:7$C2B_1$, Syt-1:7$C2B_2$, Syt-1:7$C2B_3$) and in the fourth chimera, we replaced all the loops (Syt-1:7$C2B_{123}$).

Our first goal was to investigate how the fusion properties of chromaffin granules are modified by mutations in the Syt-1 C2B domain. Chimeric proteins were overexpressed in cells with an N-terminal pHluorin (pHl) tag so that the time of fusion could be precisely identified. To facilitate polarized total internal reflection

fluorescence (pTIRF) imaging of deformations associated with fusion pore expansion, dissociated chromaffin cells were briefly exposed to the carbocyanine dye DiD to stain the plasma membrane (Anantharam *et al.*, 2010). During exocytosis, the dye diffuses from the plasma membrane into the fused granule membrane. Subsequent sequential polarized excitation of the dye (with a 561-nm p- or s-polarized laser) allows the identification of membrane topological changes that follow fusion and report on pore expansion. The p-polarized light preferentially excites DiD molecules oriented with their absorption dipole moments perpendicular to the coverglass; the s-polarized light preferentially excites DiD molecules oriented with their absorption dipole moments parallel to the coverglass (i.e., perpendicular to the plane of incidence). From *P* and *S* emissions, we calculate a *P/S* ratio and *P*+2*S* sum. The *P*+2*S* can increase or decrease depending on a variety of countervailing factors (Anantharam *et al.*, 2010). Thus, in these experiments we focus primarily on the *P/S*, which is a robust measure of membrane curvature (Anantharam *et al.*, 2010). We have previously shown that the duration of the *P/S* signal is correlated with the rate of pore expansion (Anantharam *et al.*, 2011; Rao *et al.*, 2014).

Time series of representative membrane curvature changes (i.e., *P/S*) associated with fusion of granules harboring WT and chimeric Syt proteins are shown in Figure 2, A–C. Intensity versus time graphs corresponding to images are shown on the right portion of the figure. Pooled data from many events are shown in Figure 3. As we reported previously, WT Syt-1 disperses more quickly from the site of fusion than WT Syt-7; in other words, Syt-1 fusion events are characterized by a brief fluorescence persistence time at the fusion site (PTFS) (Rao *et al.*, 2014). The PTFS was obtained by calculating the duration of the pHl signal from time 0 (defined as the frame before exocytosis and the initial fluorescence increase), to the time where the fluorescence returns to within 10% of the baseline value.

PTFS and *P/S* values ranged from 0.4 s to greater than 70 s (Figure 3). The longest events, for which there was no clear conclusion (i.e., because they lasted longer than the imaging window), were placed in the >65 s bin. However, we were still able to obtain medians for these distributions (Figure 3, black lines). For example, when pHluorin-tagged WT Syt-1 was overexpressed in cells, the median PTFS value was 11.2 s. To assess the likelihood of observing PTFS values in other groups greater than 11.2 s, we used the sign binomial test (see *Materials and Methods*). Except for the events associated with the Syt-1:7C2B$_2$ (median = 11 s; binomial probability [*p*] = 0.45) chimera, PTFS values for all other groups were different (i.e., unlikely to occur by chance) than the median PTFS value of WT Syt-1 events.

To validate the PTFS data, we overexpressed pHluorin-tagged WT Syt-1, Syt7, or Syt-1:7C2B$_{123}$ in independently prepared bovine adrenal chromaffin cells and analyzed the data with a different method. Exocytosis was evoked with 100 mM KCl or 100 µM 1,1-dimethyl-4-phenylpiperazinium iodide (DMPP), a nicotinic agonist. Fluorescence changes associated with fusion were analyzed using an algorithm developed by Bohannon *et al.* (2017). This algorithm calculates durations by curve fitting so that even long-lived fluorescence changes can be estimated. The results of this analysis are described in Supplemental Figure S1, A–E. Note that the pHluorin persistence durations shown here and in Figure 3A are not identical, but the trend is consistent with WT Syt-7 and the Syt-1 chimera dispersing more slowly from fusion sites than WT Syt-1. Using these data, the latency between stimulus application and fusion was also measured. We had previously shown that Syt-7 granules, when depolarized with elevated KCl, fused nearer to the time of stimulation than Syt-1 granules (Rao *et al.*, 2017). That observation was

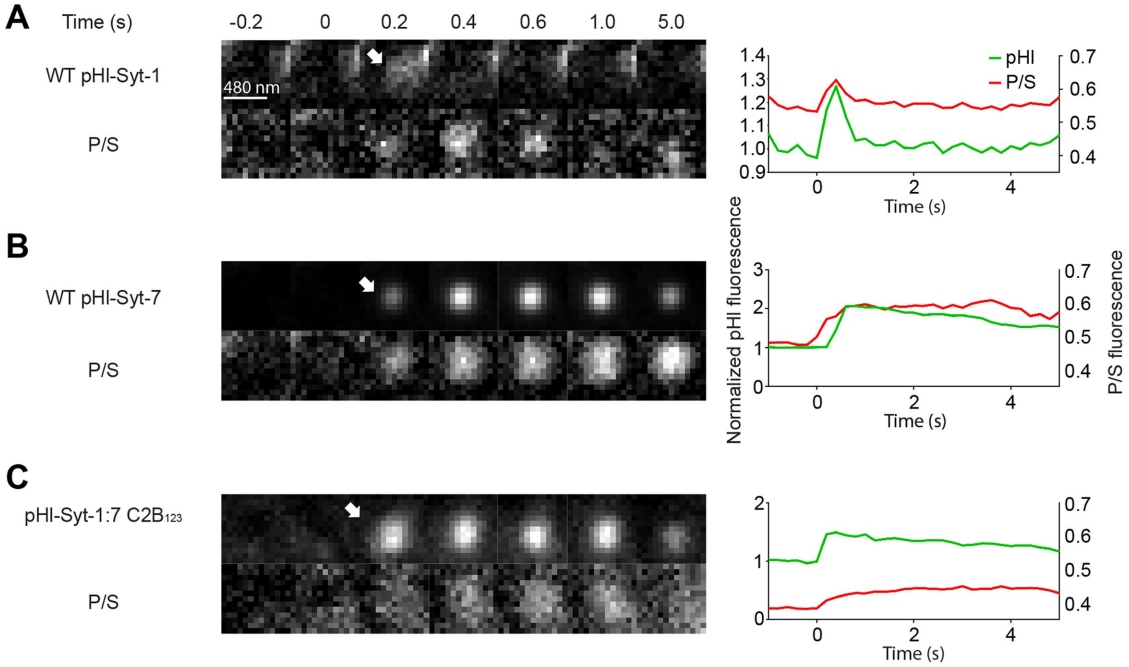

FIGURE 2: Fusion and fusion pore expansion of granules bearing WT and chimeric Syts DiD-labeled chromaffin cells were transfected with pHluorin-tagged WT Syt-1, Syt-7, or Syt-1:7C2B$_{123}$. Cells were depolarized with 56 mM KCl to elicit exocytosis. (A–C) Representative time series of fusing granules with associated membrane topological changes (*P/S*). Both the pHl and the *P/S* fluorescence intensities increase immediately on fusion. They diminish more rapidly following fusion of WT Syt-1 granules than WT Syt-7 or Syt-1:7C2B$_{123}$ granules. Fluorescence-vs.-time curves corresponding to events shown in the left panel. PHluorin fluorescence is represented by the green (left axis) curve, and *P/S* is represented by the red (right axis) curve.

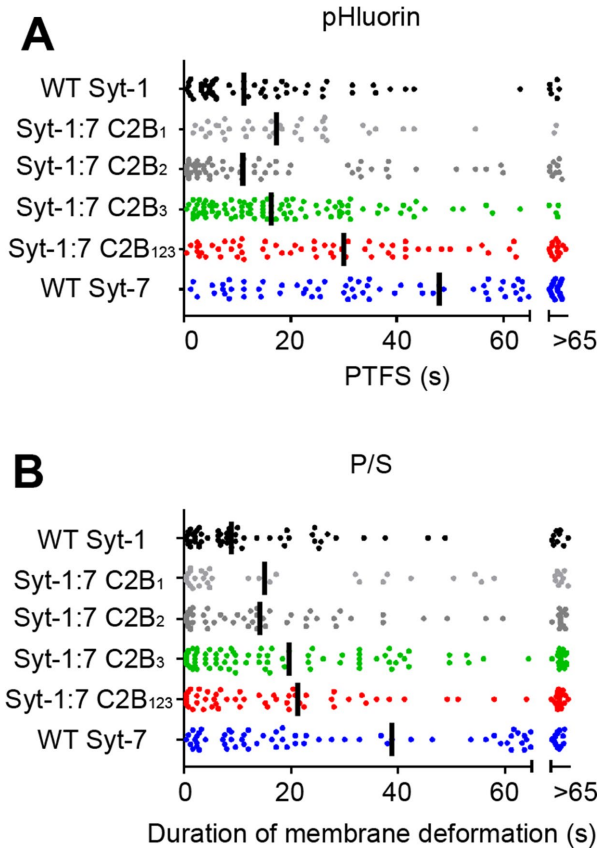

FIGURE 3: Kinetics of pore expansion and pHluorin dispersal differ between granules bearing WT and chimeric Syts. Scatter plot showing the distribution of the PTFS values (A) and the duration of membrane deformations (B) following membrane depolarization with elevated KCl. Medians are indicated by black lines. For PTFS, the medians were 11.2 s, Syt-1 WT; 17.4 s, Syt-1:7C2B1; 11.0 s, Syt-1:7C2B2; 16.4 s, Syt-1:7C2B3; 30 s, Syt-1:7C2B123; 48 s, WT Syt-7. The likelihood of observing these medians given the median PTFS for WT Syt-1 events varied. In the case of the Syt-1:7C2B2 chimera, the probability was high ($p = 0.45$). For the other chimeras, the probability was low ($p = 0.01$, Syt-1:7C2B1, $p = 0.002$, Syt-1:7C2B3; $p < 0.0001$, Syt-1:7C2B123; $p < 0.0001$, WT Syt-7). For P/S, the medians were: 8.8 s, Syt-1 WT; 15 s, Syt-1:7C2B1; 14.2 s, Syt-1:7C2B2; 19.6 s for Syt-1:7C2B3; 21.2 s, Syt-1:7C2B123; 38.8 s WT Syt-7. The likelihood of observing these medians given the median P/S for WT Syt-1 events (8.8 s) was $p < 0.0001$, Syt-1:7C2B1; $p < 0.0001$, Syt-1:7C2B2; $p < 0.0001$, Syt-1:7C2B3; $p < 0.0001$, Syt-1:7C2B123; $p < 0.0001$, WT Syt-7).

replicated here (Supplemental Figure S1F). However, there was no discernible difference in the fusion times of granules bearing Syt-1:7C2B$_{123}$ and WT Syt-1 (Supplemental Figure S1F) relative to the start of KCl stimulation.

The duration of localized membrane deformations (*P/S*) at sites of fusion of granules bearing WT or chimeric Syts was also measured (Figure 3B). The duration of *P/S* changes was more short lived for Syt-1 granule fusion events than for Syt-7 granule fusion events. The median of the distributions of the different chimeras was intermediate between WT Syt-1 (8.8 s) and WT Syt-7 (38.8 s) isoforms, with the Syt-1:7C2B$_{123}$ chimera exhibiting the slowest rates of pore expansion. Evidently, by mutating the Ca^{2+}-binding loops of the Syt-1 C2B domain, the collapse of the fused granule/plasma membrane domain—indicated by the duration of the *P/S* signal—and fluorescence dispersal of the Syt after fusion are both slowed.

The Ca^{2+}-binding loops of the Syt-1 C2B modulate the kinetics of cargo release

The *P/S* data above suggest that changes made to the C2B domain are likely to modulate the stability of the fusion pore, affecting both the rate of its expansion and the release of granule cargo proteins. To validate this idea, we coexpressed WT or chimeric Syts with NPY in chromaffin cells. Cells were depolarized with 100 mM KCl to evoke exocytosis. Localized increases in fluorescence indicated fusion of pHl-Syt labeled granules. The rate of NPY-mCherry disappearance from these granules was measured. We note that only the three loop C2B chimera was chosen for these studies, as it seemed likely to have the greatest effect on slowing pore expansion.

Representative examples of fusion events from the three different groups of coexpressed fluorescent proteins are shown in Figure 4A. Fluorescence-versus-time curves (normalized to pre-fusion fluorescence levels) for those events are shown in Figure 4B.

The "release duration" of NPY-mCherry was measured to be the time from appearance of the pHluorin signal to the time of mCherry signal disappearance. Overall, NPY was released more rapidly from granules that harbored overexpressed WT Syt-1 than either the Syt-1:7C2B$_{123}$ chimera or WT Syt-7 (Figure 4C). NPY release duration from Syt-1 granules ranged from <0.2 to 8.98 s with the median of the distribution being 0.66 s. Interestingly, its release from granules harboring Syt-1:7C2B$_{123}$ showed a wider range with slower release times, ranging from <0.2 to 9.75 s, and a higher median of the distribution (1.88 s). Granules harboring the WT pHl-Syt-7 showed the slowest release rates, ranging from 0.4 to 28 s, with the median of the distribution being 2.84 s (Figure 4C). A comparison of the release durations of NPY from granules harboring the Syt-1:7C2B$_{123}$ chimera and WT Syt-7 showed that it is significantly slower from these groups of granules than from those with WT Syt-1 (Mann–Whitney test, $p < 0.05$). On the basis of these data, we conclude that the Ca^{2+}-binding loops of the C2B domain play a significant role in determining kinetics of granule cargo release.

We have previously shown that Syt-1 and Syt-7 are usually not colocalized on granules, in the case of both endogenous and overexpressed proteins (Rao *et al.*, 2014). We were interested to know whether the overexpressed Syt-1:7C2B$_{123}$ showed a greater tendency to be cosorted with endogenous Syt-7 than overexpressed WT Syt-1. If this were the case, then any potential slowing effects of the chimera on the fusion pore could be attributed to its increased association with Syt-7. To rule out such a possibility, we transfected chromaffin cells with either GFP-Syt-1 or GFP-Syt-1:7C2B$_{123}$ and used an antibody (from SySy) to identify endogenous Syt-7 (Rao *et al.*, 2014; Jackman *et al.*, 2016). We found that roughly 6.9 ± 0.7% of overexpressed WT Syt-1 was colocalized with endogenous Syt-7 puncta, which is consistent with what we previously reported (Figure 5B) (Rao *et al.*, 2014). The C2B chimera exhibited a similarly low degree of colocalization with either endogenous (4.7 ± 1.1%) or overexpressed Syt-7 (11.1 ± 2.1%) (Figure 5B and Supplemental Figure S2).

We previously showed that a mild stimulus (e.g., 25 mM KCl) is more effective at triggering fusion of Syt-7-bearing granules than Syt-1-bearing granules (Rao *et al.*, 2014). Granules to which overexpressed Syt-1:7C2B$_{123}$ proteins are sorted are more likely to harbor endogenous Syt-1 than Syt-7 (Figure 5B). Therefore, we sought to determine whether the chimera might confer a higher fusion probability to what are ostensibly Syt-1 granules. We depolarized cells with 25 mM KCl and calculated the percentage of docked Syt-1, Syt-7, or Syt-1:7C2B$_{123}$ granules that fused (described under *Materials and Methods*). The results indicate that the fusion probability of granules harboring Syt-1:7C2B$_{123}$ is much higher than those

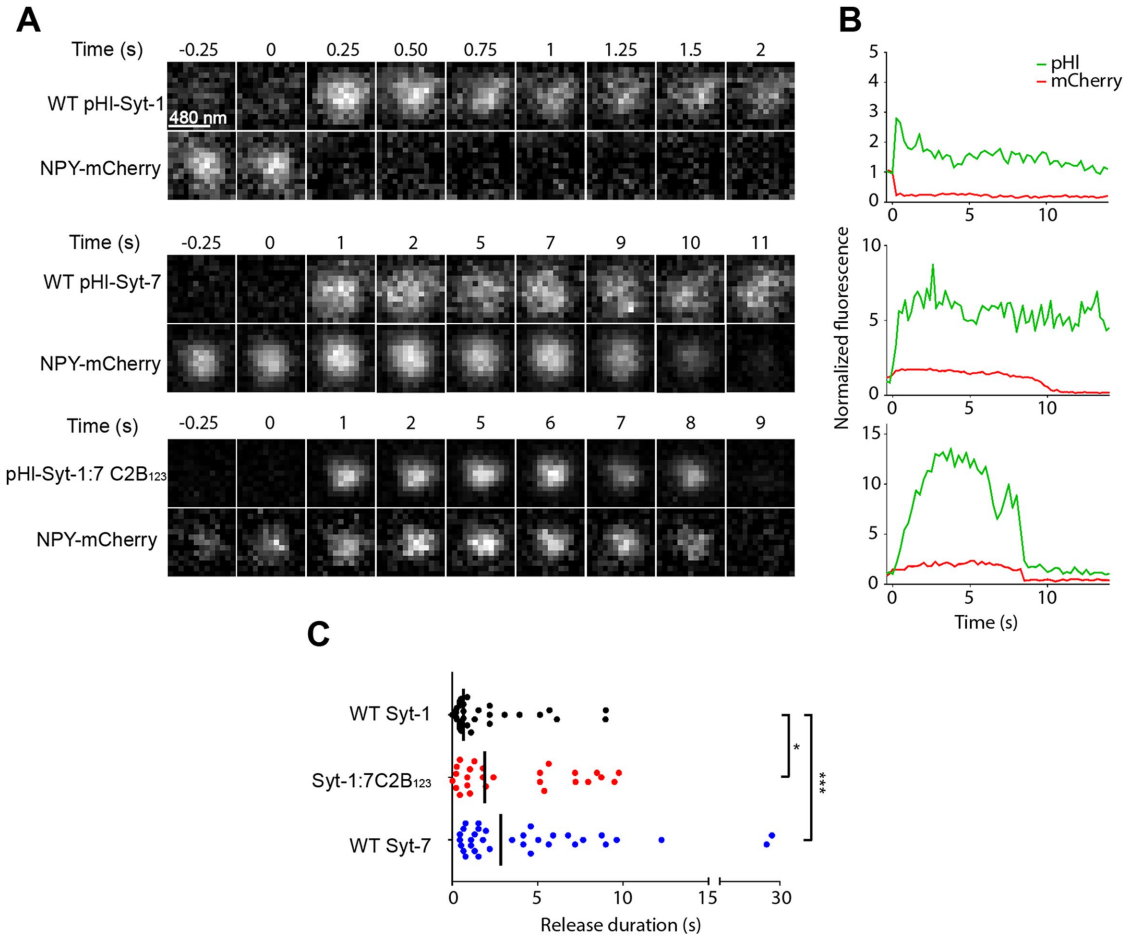

FIGURE 4: The rate of NPY discharge from granules bearing Syt-1:7C2B$_{123}$ is slower than from granules bearing WT Syt-1. Chromaffin cells were cotransfected with pHl-labeled WT Syt-1, Syt-7, or Syt1:7C2B$_{123}$ and NPY-mCherry. Depolarization was triggered via local perfusion of 100 mM KCl. (A) Representative images showing release of NPY-mCherry from fused Syt bearing granules. (B) Fluorescence-vs.-time curves for the events shown in A. (C) The release time for NPY following each fusion event is shown as a scatter plot. The solid vertical bars in C depict the median of the distribution for each isoform. Syt-1 granules discharge NPY more quickly (median, 0.66 s) than Syt-1:7C2B$_{123}$ (median, 1.9 s) or Syt-7 granules (median, 2.8 s). Differences between groups are statistically significant (*$p < 0.05$, ***$p < 0.001$, Mann–Whitney test).

harboring Syt-1 and roughly equivalent to those harboring Syt-7 (Supplemental Figure S3). One may therefore conclude that the Ca^{2+}-binding loops of the Syt-7 C2B domain partially, or perhaps wholly, control the high efficacy with which Syt-7 triggers fusion.

Mutations in the Syt-1 C2B domain modify its fusion site residence time

Our data demonstrate that the PTFS associated with fusion of WT Syt-1 granules is shorter than it is for WT Syt-7 granules. The PTFS for Syt-1:7C2B$_{123}$ falls between the WT Syts. Moreover, granules harboring Syts with a longer PTFS evince a slower rate of pore expansion and cargo release. One possible explanation for these data is that Syt-7 and Syt-1:7C2B$_{123}$ slow pore expansion by remaining at fusion sites, stabilizing the fusion pore through its membrane binding activity and thereby slowing collapse of the expanding fusion pore.

To test whether the WT Syt-7 and Syt-1:7C2B$_{123}$ exhibited a greater affinity for phospholipid membranes and/or faster dissociation kinetics than WT Syt-1, we performed steady-state lipid-binding (cosedimentation) and stopped-flow rapid-mixing experiments using the cytosolic portions of each construct (Figure 6). The steady-state lipid-binding experiments showed that all isoforms exhibit tighter binding to lipids with increasing PS, even in the absence of Ca^{2+}. Syt-7 and the Syt-1:7C2B$_{123}$ bound more avidly to liposomes than did Syt-1 at 15, 25, and 35% PS (Figure 6C), suggesting that the Syt-7 C2B loops confer a greater intrinsic affinity toward PS-containing membranes in the absence of Ca^{2+}.

For stopped-flow studies, the C2 domains of Syt proteins in the presence of Ca^{2+} and liposomes were mixed with excess chelator as shown in Figure 6D. The dissociation of the proteins from liposomes was measured by loss of FRET between donor tryptophan residues and acceptor Dansyl-PE in the liposomes. The calculated dissociation constant (k_{diss}) for the cytoplasmic domain of the Syt-1:7C2B$_{123}$ protein (180 ± 32 s^{-1}) was twofold slower than that of the WT Syt-1 C2AB (Figure 6, B and C). Notably, the k_{diss} of the WT Syt-7 C2AB is almost two orders of magnitude slower (2.34 ± 0.08 s^{-1}) than it is for WT Syt-1 (Figure 6E). These studies demonstrate that mutating these residues in C2B of Syt-1 does indeed increase the stability of Syt-membrane interactions, perhaps because of a higher intrinsic affinity for Syt-7 and the Syt-1 chimera for PS. To our knowledge, this

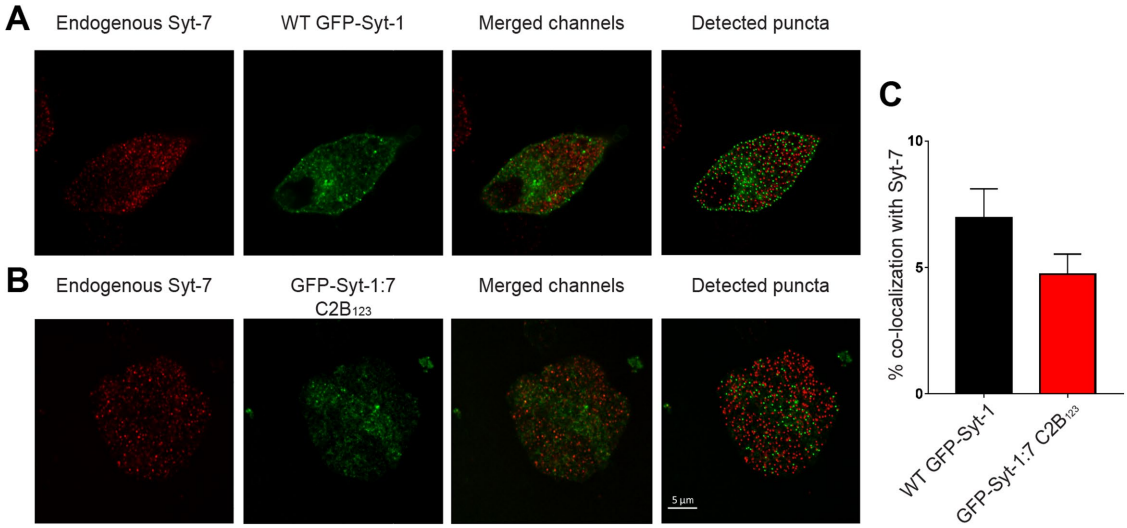

FIGURE 5: Overexpressed WT Syt-1 and Syt-1:7C2B$_{123}$ are rarely cosorted with endogenous Syt-7. Chromaffin cells were transfected with either WT GFP-Syt-1 (A) or GFP-Syt-1:7C2B$_{123}$ (B). Endogenous Syt-7 was identified with an Alexa Fluor 640 secondary antibody. Cells were imaged using confocal microscopy and granules of each color were identified using Imaris. (C) Bar graphs showing low colocalization of both WT GFP-Syt-1 and GFP-Syt-1:7C2B$_{123}$ with endogenous Syt-7. No significant difference was observed between colocalization rates with Syt-7 of the two isoforms ($p < 0.12$, Mann–Whitney test).

is the first report of a change in lipid affinity induced by a substitution of the Ca^{2+}-binding loops.

The Syt-1:7C2B$_{123}$ chimera harbors two cationic residues that are not found in WT Syt-1 in positions that could increase its affinity for anionic lipids and lead to increased membrane residence times. Surprisingly, molecular dynamics simulations suggest that these residues may also increase the number of bound Ca^{2+} ions in the chimeric C2B domain. The crystal structure of Syt7 C2B contains three Ca^{2+} in the binding pocket (and a fourth just outside), whereas the Syt1 C2B NMR structure contains only two Ca^{2+} (Fernandez *et al.*, 2001; Xue *et al.*, 2010). To examine the electrostatics of Ca^{2+} coordination by the chimera, we conducted four separate molecular dynamics simulations: one each of the WT Syt1 and chimeric C2B domains bound to two or three Ca^{2+} ions (Figure 7). For both protein forms, the two inner Ca^{2+} are well chelated by protein residues in both the 2-Ca^{2+} and 3-Ca^{2+} structures, while the third and outermost Ca^{2+} in the 3-Ca^{2+} structure is incompletely coordinated by protein, consistent with its absence in the WT crystal structure (Figure 7, A and B). One useful metric of Ca^{2+} binding from simulations is the integrated coordination number (ICN), which is a count of the average number of electronegative atoms within a defined radius of a metal center and in particular the breakdown of ICN between protein and solvent atoms (Supplemental Figure S4, A and B). The overall ICN for Ca^{2+} usually varies between 6 and 8 (Katz *et al.*, 1996). Our simulations show that the ICN values of the two inner Ca^{2+} ions were 7.0–7.9 overall and 6.0–6.9 for protein oxygens in all four simulations (Table 1). The ICN values for a third Ca^{2+} ion were 6.1–6.2 overall but only 1.1–1.2 for protein ligands, suggesting that the third Ca^{2+} binds very weakly to the WT Syt-1 and chimeric protein domains (Table 1). Interestingly, the chimeric C2B domain with 3 Ca^{2+} recruited 2 Cl^- ions from bulk solution during the simulation, which complete the coordinate shell of the outermost Ca^{2+} (Figure 7B, Table 1). In contrast, the WT Syt1 C2B domain only recruited one Cl^- ion to the Ca^{2+}-binding loops region, likely due to its lower net charge (Table 1). Another Cl^- ion was recruited in all four simulations to the lysine cluster centered on the β-4 strand, which is known to bind anionic lipids. If anion recruitment is analogous to lipid binding as suggested previously (Sutton *et al.*, 1995), then the Cl^- recruited by both WT and chimera in the 3-Ca^{2+} simulations suggests a stronger affinity for lipid membranes in the presence of the third Ca^{2+}. The fact that more Cl^- ions are recruited by the chimeric protein implies that the third Ca^{2+} could stabilize lipid binding more strongly in the chimera than in WT Syt1 C2B.

DISCUSSION

We previously showed that the chromaffin cell synaptotagmin isoforms, Syt-1 and Syt-7, were primarily sorted to different populations of granules (Rao *et al.*, 2014). Granules harboring overexpressed Syt-1 or Syt-7 tended to undergo different fusion modes and released cargos with different kinetics. More recently, we showed that Syt-1- and Syt-7-dependent fusion kinetics were largely predicted by their in vitro Ca^{2+} affinities (Rao *et al.*, 2017). The Ca^{2+} sensing ability of the synaptotagmins arises from their C2A and C2B domains. Each C2 domain consists of an eight-stranded beta sandwich with flexible loops projecting from each end (Corbalan-Garcia and Gomez-Fernandez, 2014). Three loops located on one end of each C2 domain contain conserved aspartate residues that jointly coordinate Ca^{2+} ions along with oxygen ligands from a Ser residue and carbonyl groups of the protein backbone (Zhang *et al.*, 1998; Xue *et al.*, 2010). Because the Syt isoforms have a high degree of structural similarity, even small differences in positioning, dynamics, or flexibility of the loops must be sufficient to endow a range of Ca^{2+}- and membrane-binding characteristics to the proteins. Here we sought to test this hypothesis by creating chimeras of Syt-1 and Syt-7 in which only a small number of residues within the C2B domain were modified. Because others have posited differences in the number of bound Ca^{2+} ions in the C2B between Syt-1 and Syt-7, we initially focused on this region (Xue *et al.*, 2010).

This study reveals a direct role for the C2B Ca^{2+} binding loops in controlling fusion-related properties of dense core granules. Both the complete release of peptide contents, occurring in a few seconds (Figure 4), and the collapsing of the fusion pore over tens

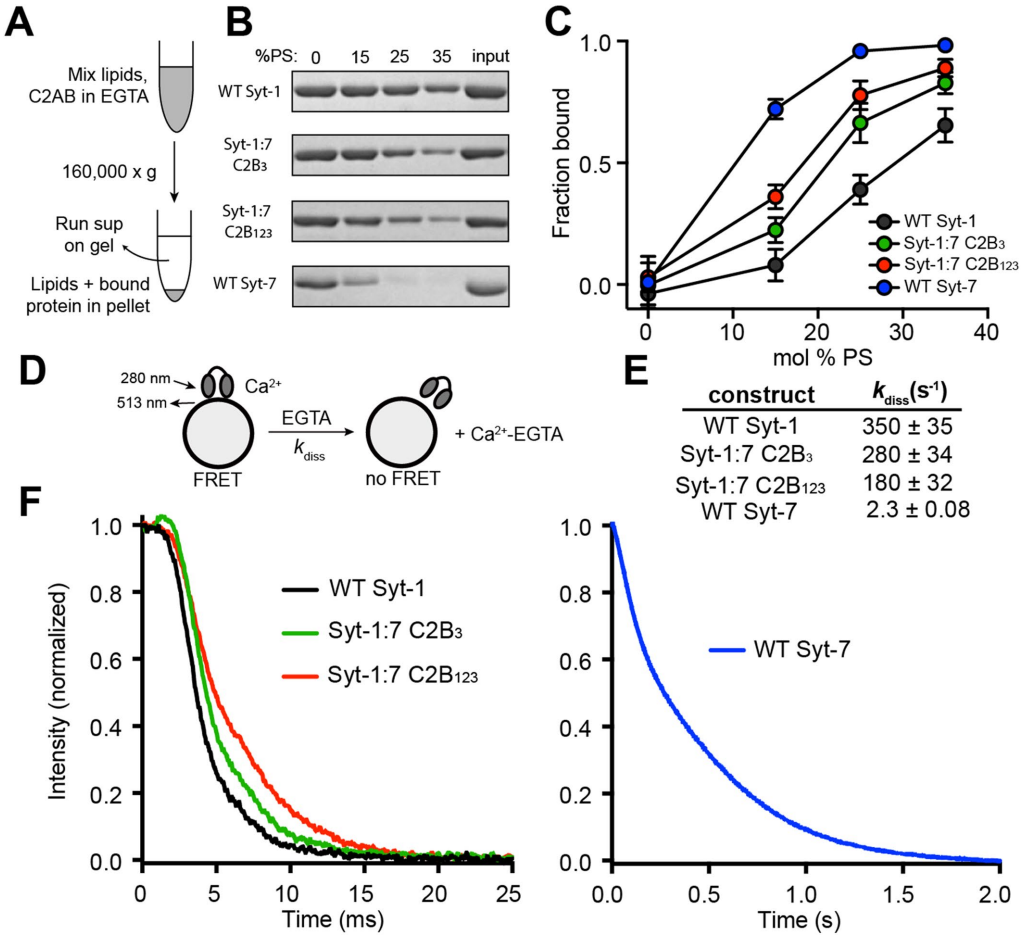

FIGURE 6: Chimeric Syts demonstrate increased affinities for phosphatidylserine. (A) Experimental scheme for steady-state lipid-binding experiments. Equilibrium binding of C2AB to PS:PC:PE liposomes was determined by measuring protein content of the unbound fraction after sedimentation of protein-liposome complexes. (B) Representative Coomassie-stained gel demonstrating dose-depending binding of Syt constructs to PS. (C) Pooled data from cosedimentation assays ($n = 4$ replicates from two independent batches). Chimeric syts demonstrate graded, intermediate affinities for PS that correspond to observed fusion pore lifetimes (WT Syt7 > Syt-1:7 $C2B_{123}$ > Syt-1:7 $C2B_3$ > WT Syt1, Mann–Whitney test). (D) Experimental scheme for stopped-flow rapid-mixing experiments to determine C2AB·Ca^{2+}·liposome complex disassembly kinetics. FRET between endogenous Trp residues in C2AB and dansyl-PE in liposomes was monitored by exciting Trp at 285 nm while measuring emission through a 470-nm long-pass filter. (E) Stopped-flow data ($n = 4$–5 experiments per construct) were fitted with single-exponential decays to determine kdiss for each C2AB construct. (F) Representative traces from stopped-flow experiments for each C2AB construct. Introduction of Syt7 Ca^{2+}-binding loops into Syt1 slowed membrane complex disassembly, but disassembly kinetics for chimeric proteins remained over an order of magnitude faster than for Syt7.

of seconds (Figures 2 and 3) are slower for Syt-7 granules than for Syt-1. Furthermore, in a chimera where all of the residues that form the three C2B domain Ca^{2+}-binding loops were mutated (Syt-1:7 $C2B_{123}$), the PTFS—ostensibly related to the rate at which the Syt C2AB "releases" the target membrane—is extended compared with WT Syt-1. This effect indicates that some aspect of the observed differences in pore expansion rates between isoforms must be due to properties endowed by these loops.

Our in vitro and in silico data support a mechanism by which the loops may modulate pore mechanics, namely that Syt C2 domain-lipid contacts control to a large extent the overall rate of expansion from the initial pore (Figure 8). In this model, the fusion pore expansion rate is at least partly governed by dissociation rates of Syt C2A and C2B domains from the highly curved membrane at the fusion pore neck. Results from the biochemical studies and molecular dynamics simulations suggest that the chimeric Syt-1:7 $C2B_{123}$ domain has a higher affinity for anionic phospholipids than the WT Syt-1 C2B domain (Figure 6). This chimeric C2B domain dissociates more slowly than WT Syt-1 C2B domain by a factor of ~2, which is similar to the two- to threefold slower fusion pore expansion rates we observe with this mutant. We also note that the rank orders of the increased affinity for PS and decreasing dissociation rate in these constructs matches the rank order of the kinetic changes at the fusion site (Figures 2 and 6). This difference could be due to the presence of R333 and K364, which may enable the chimeric protein to bind better anionic phospholipids in a manner analogous to their ability to recruit Cl^- ions in our simulations. Also, the increased hydrophobic surface contributed by the isoleucine on the membrane-proximal tip of Syt-7 Loop 1 is worth ~0.5 kcal/mol in membrane insertion free energy relative to the valine on Syt-1 and may contribute to the

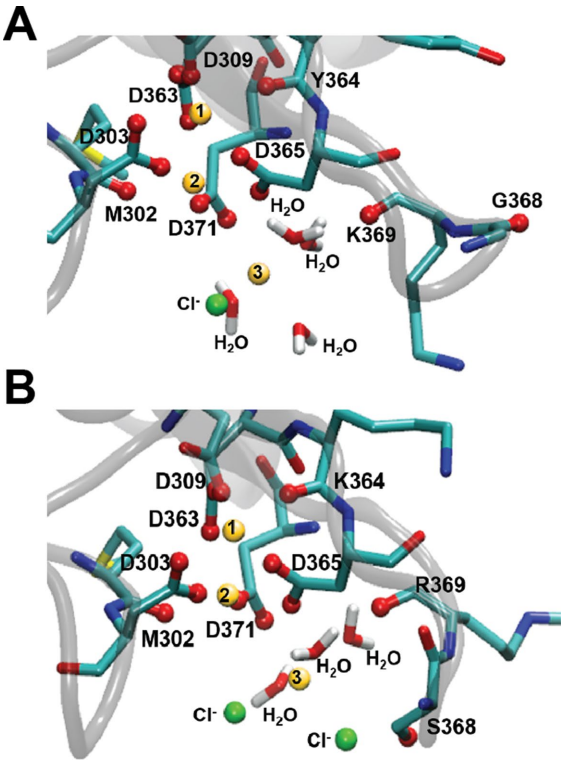

FIGURE 7: Computational model for Ca^{2+} and Cl^- binding in WT and chimeric Syt-1. Equilibrated structure overviews of three Ca^{2+} ions in the binding sites of (A) Syt-1 C2B WT and (B) Syt-1:7C2B$_{123}$ models. The proteins are shown in cartoon format with colors in gray; Ca^{2+} and Cl^- ions are yellow and green spheres, respectively, with their surrounding residues and water molecules shown as licorice (cyan, C; blue, N; red, O; yellow, S; white, H); and the O atoms coordinating the Ca^{2+} ions are highlighted as red spheres. For clarity, protein H atoms are not shown.

Simulation	Ligand	1st Ca^{2+}	2nd Ca^{2+}	3rd Ca^{2+}
WT 2 Ca^{2+}	Protein O	6.9	6.0	
	Water O	1.0	1.0	
	Cl^-	0.0	0.0	
	Sum	**7.9**	**7.0**	
WT 3 Ca^{2+}	Protein O	6.9	6.0	1.2
	Water O	1.0	1.0	4.0
	Cl^-	0.0	0.0	1.0
	Sum	**7.9**	**7.0**	**6.2**
CH 2 Ca^{2+}	Protein O	6.9	6.0	
	Water O	1.0	1.0	
	Cl^-	0.0	0.0	
	Sum	**7.9**	**7.0**	
CH 3 Ca^{2+}	Protein O	6.9	6.0	1.1
	Water O	1.0	1.0	3.0
	Cl^-	0.0	0.0	2.0
	Sum	**7.9**	**7.0**	**6.1**

TABLE 1: Integrated coordination numbers for the first solvation shell ($r \leq 3.25$ Å) for Ca^{2+} in each simulation (CH denotes Syt-1:7 C2B$_{123}$).

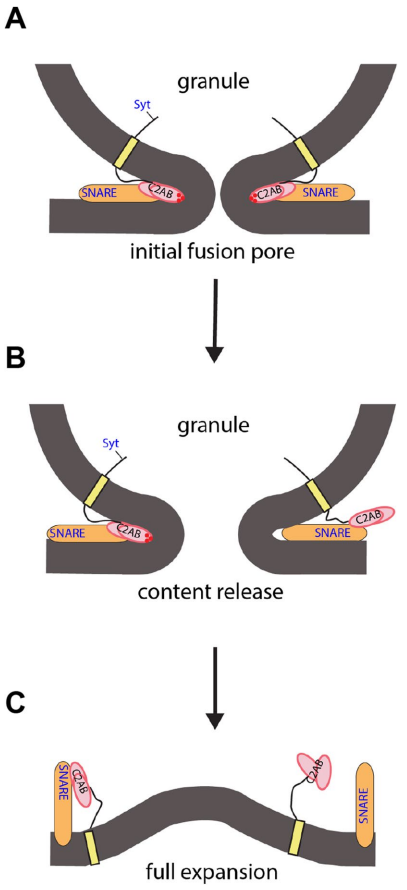

FIGURE 8: Syt-centric model of fusion pore expansion. (A) On initial fusion mediated by Ca^{2+}-triggered membrane insertion of Syt C2 domains (pink ovals) and zippering of SNARE proteins (orange), the narrow fusion pore ring is lined by membrane-bound Syt, SNARE, and other SM proteins (not shown for clarity). (B) As Syt C2 domains begin to dissociate from the membrane, the fusion pore expands, allowing content release. Relative rates of this step: Syt1 > CH ≈ Syt7. (C) As Syt C2 domains continue to dissociate from the membrane, the fusion pore continues to expand until the Syt TM regions (yellow rectangles) can diffuse away from the fusion site. At this point, Syt may or may not remain bound to SNARE proteins for sorting into recycling endosomes. Relative rates of this step: Syt-1 > CH > Syt-7. (CH denotes Syt-1:7 C2B$_{123}$.)

difference in dissociation kinetics (Wimley and White, 1996). Together, the ordinal correlation of PS binding and dissociation rate with the cellular measurements strongly suggests that these properties play an important role in modulating fusion pore kinetics.

There are some similarities between this study and one that was previously conducted by Rizo and colleagues (Xue *et al.*, 2010). In the aforementioned work, chimeras were generated in which the Syt-1 C2B domain was replaced entirely with the Syt-7 C2B domain. Portions of the Syt-7 C2B were then reverted back to the Syt-1 backbone via mutagenesis. When the entire Syt-1 C2B domain was replaced with the Syt-7 C2B, a significant reduction in the amplitude of postsynaptic electrical signaling was observed. None of the reversions could rescue the apparent loss of exocytosis. In our study, we employed a different approach. The chimeras we generated are almost identical to WT Syt-1, excluding a handful of residues that differentiate the Syt-1 C2B loops from corresponding Syt-7 loops. In our system, there were no apparent deficits in exocytosis due to overexpression of the chimeras.

In the presence of Ca^{2+}, Syt-1 can bind the t-SNARE proteins syntaxin and SNAP-25, and these interactions have been shown to be C2B dependent and critical for exocytosis to proceed properly (Bai *et al.*, 2004b; Zhang *et al.*, 2010; Mohrmann *et al.*, 2013; Weber *et al.*, 2014; Schupp *et al.*, 2016). Therefore, it has been suggested that the Syt C2B might create a scaffold for the recruitment and proper assembly of SNARE complexes (Littleton *et al.*, 2001). Furthermore, Syt-SNARE binding also appears to influence fusion pore stability, as impairment of t-SNARE binding inhibits fusion pore expansion and promotes kiss-and-run exocytosis (Lynch *et al.*, 2008). This raises the question of whether Syt-1 and Syt-7 differ in their affinity for binding proteins and not just phospholipids, as previously shown (Sugita and Sudhof, 2000). For example, the tendency of chimeras Syt1:7-$C2B_3$ and Syt1:7-$C2B_{123}$ (as well as WT Syt-7) to mediate events in which the fusion pore expands more slowly could be partially due to altered interactions with t-SNAREs. This is a possibility we cannot yet rule out. However, because no changes were made to residues implicated in binding the SNARE bundle, the chimeras are unlikely to modulate pore properties via their interaction with SNAREs (Zhou *et al.*, 2017).

In summary, this study demonstrates that the Syt-1 C2B domain Ca^{2+}-binding loops influence the protein's persistence at exocytotic sites after fusion and the likelihood of fusion pores undergoing rapid expansion during exocytosis. Substitution of all three Syt-1 C2B Ca^{2+}-binding loops resulted in a pronounced shift in fusion properties of Syt-1 toward those of WT Syt-7. It should be noted that this chimera is not a phenocopy of Syt-7, which suggests that other regions of Syt are likely to contribute in important ways to the various fusion-related properties we investigated. Indeed, we and others have shown that the C2A domain also binds membranes more strongly and dissociates more slowly in Syt-7 than Syt-1 (Sugita *et al.*, 2002; Tucker *et al.*, 2003; Brandt *et al.*, 2012; Voleti *et al.*, 2017). The large difference in membrane dissociation kinetics between chimera and WT Syt-7 C2AB tandem domains (Figure 6E) also suggest that the C2A domain plays an important role, and future studies of fusion pore expansion rates with C2A chimeras are planned. Nonetheless, our present results provide novel mechanistic insights into how the Syt-1 C2B domain regulates the later stages of exocytosis via modulation of fusion pore properties.

MATERIALS AND METHODS

Generation of chimeric synaptotagmin DNA constructs

Synaptotagmin chimeras were generated using site-directed mutagenesis. For chimeras Syt-1:7$C2B_1$, Syt-1:7$C2B_2$, and Syt-1:7$C2B_3$, wild-type Syt-1 pHluorin in the pCI vector was PCR amplified with primer sets designed to mutate each rat Syt-1 C2B loop to match the corresponding C2B loop of rat wild-type Syt-7 (Supplemental Table S1). The resulting amino acid substitutions for each construct are as follows: Syt-1:7$C2B_1$: K301A, V304I, L307T; Syt-1:7$C2B_2$: N333R, T334N; Syt-1:*7C2B3*: Y364K, I367L, G368S, and K369R. Chimera Syt-1:7$C2B_{123}$ contains all of the above mutations and was generated by performing two additional rounds of mutagenesis; first, Syt-1:7$C2B_1$ was used as a template to mutate C2B loop 2, and then this product (Syt-1:7$C2B_{12}$) was used as the template in a second reaction to mutate C2B loop 3. Following PCR, all products were treated with *Dpn*I restriction endonuclease (New England Biolabs, Ipswich, MA) to digest the template DNA, ligated, and transformed into DH5α competent cells (Thermo Fisher Scientific, Waltham, MA). Proper mutagenesis was confirmed using two subsequent rounds of Sanger sequencing (Applied Genomics Technology Center, Detroit, MI).

Chromaffin cell preparation and transfection

Chromaffin cells were isolated from the adrenal medullae of adult cows (*Bos taurus*) obtained from JBS Packing Company (Plainwell, MI). Transient transfections were performed as described earlier (Rao *et al.*, 2014). Briefly, cells were plated on 35-mm glass-bottom tissue culture dishes (refractive index, 1.51; World Precision Instruments, Sarasota, FL) precoated with poly-D-lysine and bovine collagen. Cells were transiently transfected with plasmid(s) by electroporation using the Neon transfection system (Invitrogen, Carlsbad, CA) with a single pulse of 1100 mV for a period of 40 ms. PHluorin-(pHl) or GFP-tagged WT Syt-1, WT Syt-7, or one of the chimeric Syt-1 constructs were transfected separately for experiments measuring fusion probability or protein persistence time at fusion sites. Two additional groups of cells were transfected with one of the pHl-tagged constructs. The first group of cells was labeled with DiD and used to investigate the membrane curvature using polarized pTIRF imaging (Anantharam *et al.*, 2010). The second group of cells was cotransfected with mCherry-tagged neuropeptide Y (NPY) to investigate the rate of cargo release from granules harboring each of the overexpressed pHl-tagged Syt isoforms using TIRF imaging. Last, GFP-tagged Syt-1:7$C2B_{123}$ was cotransfected with either mOrange2 tagged WT Syt-1 or WT Syt-7 to investigate protein sorting. For single or double transfections, the amount of total DNA was 15 ng/10^6 cells. Following plating, the media was changed after overnight incubation and all experiments were performed 48–120 h following transfection to ensure expression of the fusion proteins. All procedures were performed following approval from the University of Michigan Institutional Animal Care and Use Committee (IACUC).

TIRF microscopy

A detailed description of the polarized TIRF setup is detailed elsewhere (Passmore *et al.*, 2014). Briefly, imaging was performed on an inverted microscope (IX81; Olympus, Center Valley, PA) equipped with a 60× oil-immersion objective (NA 1.49), two additional lenses (1.6× and 2×) in the emission path between the microscope and a cooled electron-multiplying charge-coupled device camera (iXon3; Andor Technology, South Windsor, CT). Two-color TIRF microscopy was performed by illuminating the samples using a 488-nm argon ion laser and a p- and s-polarized 561-nm solid-state Sapphire Coherent laser (Santa Clara, CA). Lambda SC smart-shutter controllers have been employed for rapid switching between the excitation wavelengths (Sutter Instruments, Novato, CA). Images were acquired with Metamorph software (Molecular Devices, LLC, Sunnyvale, CA) successively in the green and the red channels with an exposure time of 30 ms and an EM gain of 300. The frame acquisition rate was ~4–5 Hz for a pair of images. The frame final pixel size was ~80 nm.

Immunocytochemistry

Immunofluorescence microscopy was performed to detect the distribution of endogenous Syt-7 with respect to overexpressed GFP-Syt-1 or GFP-Syt-1:7$C2B_{123}$ within chromaffin cells. Chromaffin cells plated on a precoated 35 mm glass-bottom cover dish were stained with an antibody for Syt-7 (Rao *et al.*, 2014). The cells were first fixed with 4% paraformaldehyde in Sorensen's buffer for 30 min at 37°C. The cells were quickly rinsed following the incubation and quenched using a solution of 50 mM NH_4Cl in phosphate-buffered saline and incubated again for 30 min at 37°C. After washing off the quenching solution, the cells were permeabilized using acetone solution for 7 min. After the incubation, the cells were washed with Tris-buffered saline (TBS) twice and blocked with 0.01% gelatin in TBS for 30 min

followed by 4% donkey serum for 30 min, both at 37°C. A solution of 2 mg/ml bovine serum albumin (BSA) made in TBS was used to dilute the primary and secondary antibodies (1:400 for both primary and secondary). Cells were incubated for 2 h at 37°C with a polyclonal rabbit anti-Syt-7 antibody (Cat. No. 105 173) from Synaptic Systems, Göttingen, Germany. Following incubation, the cells were washed five times with TBS and incubated for 70 min with Alexa-conjugated anti-rabbit and anti-mouse secondary antibodies (Molecular Probes/Invitrogen, Eugene, OR). Finally, the cells were washed five times following the secondary antibody incubation and imaged by confocal microscopy (Nikon A1, Zeiss 880).

Cell stimulation

All TIRF experiments were performed at room temperature in pre-warmed PSS (physiological salt solution) containing 145 mM NaCl, 5.6 mM KCl, 2.2 mM $CaCl_2$, 0.5 mM $MgCl_2$, 5.6 mM glucose, and 15 mM HEPES, pH 7.4. Chromaffin cells that were used for pTIRF were stained with DiD diluted in PSS 1:200 for 30 s and washed with PSS. Individual cells were stimulated using a needle (100-µm inner diameter) connected to a perfusion system under positive pressure ALA-VM4 (ALA Scientific Instruments, Westbury, NY). Cells were perfused with PSS for 5 s and then stimulated with high potassium containing solution (either 56 or 100 mM KCl) for 70 s or 100 µM (Sigma-Aldrich) diluted in PSS for 2 s to trigger exocytosis.

Image analysis

Images for pTIRF experiments were captured sequentially using Metamorph software (Molecular Devices, LLC, Sunnyvale, CA). Individual granules undergoing exocytosis were evident by an increase in the pHluorin intensity following fusion with the plasma membrane as a result of change in pH from acidic to neutral. Changes in the fluorescence intensity versus time for the different fusion events were calculated using custom software written in IDL (ITT, Boulder, CO).

For pTIRF, image sequences for each channel (488, p-pol 561, s-pol 561) were processed pixel by pixel using a custom IDL script to produce three types of image stacks: a 488 Syt-pHl, a *P/S* ratio intensity stack, and a *P+2S* stack. Before generating the *P/S* and *P+2S* stacks, raw intensity values for the *P* and *S* emission images were normalized against rhodamine 6G sample images. Unlike DiD, the rhodamine 6G solution used for normalization can be assumed to contain randomly oriented dye molecules, and thus it can report on differences in the intensity of the incoming polarized light beams.

From these three types of image stacks, individual fusion event regions of interest (ROIs) (~240-nm radius) were manually selected for analysis based on the sudden increase in pHluorin fluorescence that occurs due to neutralization of the secretory granule lumen upon fusion pore opening. Event durations based on the pHl and *P/S* stacks were calculated by plotting the fluorescence intensity against time and measuring the number of frames (converted to seconds) that the intensity remained above 10% of the prefusion baseline value. The baseline was calculated as the average ROI intensity in the three frames immediately prior to the rise in pHl intensity associated with an event. Only events in which both the pHl and *P/S* signatures rose above 10% of their respective baselines within five frames of each other were included for analysis.

For multichannel imaging of cargo release (pHl-Syt and NPY-mCherry), experiments were performed on a line-line Olympus cellTIRF (Waltham, MA) system described elsewhere (Rao *et al.*, 2017). Emission signals were separated with an Optosplit (CAIRN Research, UK) and analyzed individually. Fusion events were processed using a custom IDL script that identifies colocalized pHl appearance and mCherry disappearance in two different channels. The ROIs were selected at pHl fusion spots where colocalized NPY puncta were observed prior to granule fusion (determined by the beginning of the pHl signal). mCherry fluorescence values were normalized to baseline (1 s before fusion) and fluorescence traces were plotted after fusion. Release time was counted from the rise of the pHl signal until the total disappearance of the mCherry signal.

Granules bearing fluorescent Syts that were present in the evanescent field at the start of stimulation were considered to be "docked." The number of fusing granules after KCl depolarization was divided by the number of docked granules to obtain a measure of "fusion probability." Fusion events were identified by an increase in GFP fluorescence of greater than 20% (Rao *et al.*, 2017). Granules that moved into the evanescent field after stimulation were not included in the analysis, regardless of whether they subsequently fused. For docked granule fusion analysis, ImageJ (National Institutes of Health, Bethesda, MD) was used.

Images obtained from confocal microscopy were analyzed with Imaris software (Bitplane, Zurich, Switzerland) using the "spot function" module for object based colocalization analysis.

Statistical analysis

Figures and statistical analysis were performed using Prism 7.00 (GraphPad Software, La Jolla, CA). Where possible, the Mann–Whitney test was used to assess whether differences in pHluorin persistence times or cargo release times were significantly different between groups. For the data set from which Figures 2 and 3 were made, increases in pHluorin and DiD fluorescence associated with fusion sometimes persisted beyond the imaging window (>65 s). Therefore, nonparametric statistical tests such as the Mann–Whitney could not be applied. Instead, we used the sign binomial test to calculate the likelihood (*p* value) of encountering persistence time at the fusion site (PTFS) and *P/S* values that deviate from the corresponding WT Syt-1 medians. (GraphPad software web site www.graphpad.com/quickcalcs/binomial1.cfm). In effect, this test determines the probability of an outcome given a theoretical probability of "success." Here is an example of how this test was applied. We calculated that the median *P/S* for WT Syt-1 events was 8.8 s (Figure 3B). To determine the likelihood of WT Syt-7 event durations being greater than 8.8 s, we counted the number of successes (69 Syt-7 *P/S* events had durations greater than 8.8 s) and the total number of "trials" (89 Syt-7 *P/S* events were recorded). If the probability of success is 0.5, given 69 "successes" in 89 "trials," then the one-tail *p* value is <0.0001.

An additional automated image analysis procedure was used to calculate Syt-pHl fluorescence duration using an IDL program named "secrate3" (Bohannon *et al.*, 2017). After a user selects fusion events from blinded files, the program generates fluorescence-versus-time curves for each one. A user to selects a start time, t_{start}, just before fluorescence begins and an end time, t_{end}, when fluorescence returns to baseline. The PTFS, of the event is obtained via fitting a weighted polynomial to the data and projecting the time spent above the prefusion baseline fluorescence, described in detail elsewhere (Bohannon *et al.*, 2017). Importantly, PTFS that last longer than the imaging period can still be extrapolated by the fitting method.

Protein purification

C2AB modules from Syt-1 and Syt-7 chimeras (amino acids 96–421) were subcloned into a pGEX4T vector (GE), expressed as GST-fusion proteins, purified from *Escherichia coli* lysates via GST-sepharose affinity chromatography, and thrombin cleaved in

100 mM KCl, 25 mM HEPES, pH 7.4, 5% glycerol. Syt7 C2AB (amino acids 134–403) was expressed with a His_6 tag (pTrcHis vector, Invitrogen), purified from *E. coli* lysates via Ni-NTA-sepharose affinity chromatography, eluted with 500 mM imidazole, and dialyzed overnight against 100 mM KCl, 25 mM HEPES, pH 7.4, 5% glycerol. Protein concentrations were determined by SDS–PAGE using BSA standards.

Liposome preparation

Lipid films were formed by evaporating chloroform solutions of phospholipids under a stream of nitrogen. For stopped-flow rapid mixing experiments, liposomes contained (in %mol/mol) 45 POPC, 25 POPE, 25 DOPS, 5 Dansyl-PE. For PS titrations, liposomes contained (in % mol/mol) 35-75 POPC, 30 POPE, and 0-35 DOPS, with DOPS replacing POPC in equimolar quantities. Films were dried under vacuum for 2 h and then rehydrated for 30 min in buffer containing 100 mM KCl, 25 mM HEPES-NaOH, pH 7.4, for a final concentration of 10 mM [lipid]. Liposomes were obtained by extruding this mixture 31 times through a 100-nm polycarbonate filter (Whatman).

Stopped-flow rapid mixing experiments

A mixture of 4 μM C2AB, 200 μM $CaCl_2$, and 250 μM lipid was combined in buffer containing 100 mM KCl, 25 mM HEPES, pH 7.4. This mixture was loaded into one syringe of an SX-18.MV stopped-flow spectrometer (Applied Photophysics) held at 14°C and rapidly mixed with an equal volume of 5 mM ethylene glycol-bis(2-aminoethyl ether)-*N*,*N*,*N*′,*N*′-tetraacetic acid (EGTA) in the same buffer. Samples were allowed to equilibrate in the spectrometer for 5 min prior to mixing. Excitation at 285 nm was provided via xenon arc lamp and monochromator (Applied Photophysics), and emission was monitored via photomultiplier tube through a 470-nm long-pass filter (KV470, Schott). Data were collected at 40 kHz for 0.1 s (Syt1 and chimeras) or 2 kHz for 2 s (Syt7). Single-exponential decays were fitted using Prism (GraphPad) prior to normalization, with the first 2 ms of each trace omitted from analysis to account for instrument dead time.

Equilibrium cosedimentation assays

Liposomes (2 mM total lipid), C2AB (4 μM), and EGTA (0.2 mM) were combined in 100 μl buffer containing 100 mM KCl, 25 mM HEPES-NaOH, pH 7.4. The mixture was incubated for 15 min at room temperature with shaking, loaded into a polycarbonate centrifuge tube, and centrifuged at 65,000 rpm for 30 min in a TLA-100 rotor (Beckman). An aliquot of the supernatant was combined 1:1 with 2× SDS sample buffer and subject to SDS–PAGE. Gels were stained with Coomassie blue and the bands quantified using ImageJ.

Computational methods

We have built two models of the WT Syt-1 C2B domain and two models of the chimeric C2B domain, where $2Ca^{2+}$ and $3Ca^{2+}$ indicate, respectively, that 2 and 3 Ca^{2+} ions bind in the Ca^{2+}-binding site formed by the loops. For Syt-1 $2Ca^{2+}$, the first model in the NMR structure of Syt-1 C2B (PDB code 1K5W [Fernandez *et al.*, 2001]), which contains two Ca^{2+} ions, was employed. The Syt-1 $3Ca^{2+}$ model was constructed by superimposing Syt-1 $2Ca^{2+}$ with the crystal structure of Syt-7 C2B (PDB code 2N5A [Xue *et al.*, 2010]) followed by adding the third Ca^{2+} ion in the Syt-7 binding site to Syt-1 $2Ca^{2+}$; this was possible because the binding conformations of the first two Ca^{2+} ions are very similar in both Syt-1 and Syt-7. For CH $3Ca^{2+}$, a homologous protein model was built from the amino acid sequence using the Swiss-Model (Biasini *et al.*, 2014) program taking Syt-1 $3Ca^{2+}$ as a template. Comparing the CH and Syt-1 models, the "bodies" are taking essentially the same conformations, but the loops (especially CBL3) differ noticeably. Roughly speaking, the orientation of the CH loops is between those of WT Syt-1 and WT Syt-7. As expected, the Ca^{2+} binding conformations in the initial geometry of CH $3Ca^{2+}$ are similar to those in WT Syt-7: the first Ca^{2+} is held by the O atoms of D303, D309, D363, and D365 side chains and of the K364 backbone; the second Ca^{2+} by the D303, D363, D365, and D371 side chains and the M302 backbone; and the third Ca^{2+} by the D365, S368, and D371 side chains and the R369 backbone. As explained under the *Results* and *Discussion* sections, the equilibrated geometry of CH $3Ca^{2+}$, however, revealed a binding conformation for the third Ca^{2+} quite different from that in the initial geometry. Consequently, the CH $2Ca^{2+}$ model was obtained by deleting the third Ca^{2+} ion from the 100-ns equilibrated CH $3Ca^{2+}$ model (see below).

The proteins were solvated in 0.15 M of KCl solution. The systems are described by the Charmm22 force fields with the ϕ, ψ dihedral cross-terms or grid-based energy maps (CMAP) corrections (MacKerell *et al.*, 1998; Mackerell *et al.*, 2004) and the TIP3P (Jorgensen *et al.*, 1983) water model. Periodic boundary was employed, where the primary cubic box contained a protein, two or three Ca^{2+} ions, ~25,000 water molecules, ~70 K^+ ions, and ~85 Cl^- ions (the exact numbers of the K^+ and Cl^- ions varied between models for maintaining charge neutrality). A model system was minimized for 5000 steps followed by a "heating-up" molecular dynamics (MD) simulation where the temperature was gradually increased from 0 to 298 K in 2 ns. During the first 1 ns, the backbone heavy atoms (N, C, O, and Cα) were held fixed to their spatial positions, and the solvation shells of the Ca^{2+} ions were retained by imposing harmonic restraints to the O–Ca distances. The constraints on the backbone atoms were released in the second half of the heating-up process. A final equilibration of 100 ns was then conducted under the *NpT* ensemble at $p = 1$ bar and $T = 298$ K without any constraint or restraint. We found that the Ca^{2+} binding in the $2Ca^{2+}$ models appeared to be very stable. In the $3Ca^{2+}$ models, there were significant changes to the third Ca^{2+} binding geometries during the first 20 ns, while the first and second Ca^{2+} binding geometries remained largely unperturbed throughout the entire simulations. Analysis (e.g., on the protein backbone RMSD values) suggested that the proteins were fully equilibrated after 60 ns; to be on the safe side, however, only the last 20 ns of the trajectories was used for the final analysis of the radial distribution functions and ICN.

The model visualization, manipulation, and analysis were performed by using VMD (Humphrey *et al.*, 1996) 1.9.3, supplemented by in-house scripts, and the dynamics simulations were carried out by using Nanoscale Molecular Dynamics (NAMD) program (Phillips *et al.*, 2005) 2.10.

ACKNOWLEDGMENTS

We thank Ronald W. Holz for suggestions on bovine adrenal cell preps and data analysis. This research was supported by the National Institutes of Health (GM111997 to A.A., MH061876 to E.R.C., and GM102866 to J.D.K.), the Camille and Henry Dreyfus Foundation (TH-14-028 to H.L.), and the American Heart Association (SDG14420049 to A.A.). This work used XSEDE under grant CHE-140070, supported by National Science Foundation grant number ACI-1053575, and the National Energy Research Scientific Computing Center under grant m2495. E.R.C. is an Investigator of the Howard Hughes Medical Institute.

REFERENCES

Anantharam A, Bittner MA, Aikman RL, Stuenkel EL, Schmid SL, Axelrod D, Holz RW (2011). A new role for the dynamin GTPase in the regulation of fusion pore expansion. Mol Biol Cell 22, 1907–1918.

Anantharam A, Onoa B, Edwards RH, Holz RW, Axelrod D (2010). Localized topological changes of the plasma membrane upon exocytosis visualized by polarized TIRFM. J Cell Biol 188, 415–428.
Bacaj T, Wu D, Yang X, Morishita W, Zhou P, Xu W, Malenka RC, Sudhof TC (2013). Synaptotagmin-1 and synaptotagmin-7 trigger synchronous and asynchronous phases of neurotransmitter release. Neuron 80, 947–959.
Bai J, Tucker WC, Chapman ER (2004a). PIP2 increases the speed of response of synaptotagmin and steers its membrane-penetration activity toward the plasma membrane. Nat Struct Mol Biol 11, 36–44.
Bai J, Wang CT, Richards DA, Jackson MB, Chapman ER (2004b). Fusion pore dynamics are regulated by synaptotagmin*t-SNARE interactions. Neuron 41, 929–942.
Bhalla A, Tucker WC, Chapman ER (2005). Synaptotagmin isoforms couple distinct ranges of Ca2+, Ba2+, and Sr2+ concentration to SNARE-mediated membrane fusion. Mol Biol Cell 16, 4755–4764.
Biasini M, Bienert S, Waterhouse A, Arnold K, Studer G, Schmidt T, Kiefer F, Cassarino TG, Bertoni M, Bordoli L, *et al.* (2014). SWISS-MODEL: modelling protein tertiary and quaternary structure using evolutionary information. Nucleic Acids Res 42, W252–W258.
Bohannon KP, Bittner MA, Lawrence DA, Axelrod D, Holz RW (2017). Slow fusion pore expansion creates a unique reaction chamber for co-packaged cargo. J Gen Physiol 149, 921–934.
Brandt DS, Coffman MD, Falke JJ, Knight JD (2012). Hydrophobic contributions to the membrane docking of synaptotagmin 7 C2A domain: mechanistic contrast between isoforms 1 and 7. Biochemistry 51, 7654–7664.
Carmichael SW, Winkler H (1985). The adrenal chromaffin cell. Sci Am 253, 40–49.
Chapman ER (2008). How does synaptotagmin trigger neurotransmitter release? Annu Rev Biochem 77, 615–641.
Cheng Y, Sequeira SM, Malinina L, Tereshko V, Sollner TH, Patel DJ (2004). Crystallographic identification of Ca2+ and Sr2+ coordination sites in synaptotagmin I C2B domain. Protein Sci 13, 2665–2672.
Corbalan-Garcia S, Gomez-Fernandez JC (2014). Signaling through C2 domains: more than one lipid target. Biochim Biophys Acta 1838, 1536–1547.
Douglas WW (1968). Stimulus-secretion coupling: the concept and clues from chromaffin and other cells. Br J Pharmacol 34, 451–474.
Fernandez I, Arac D, Ubach J, Gerber SH, Shin O, Gao Y, Anderson RG, Sudhof TC, Rizo J (2001). Three-dimensional structure of the synaptotagmin 1 C2B-domain: synaptotagmin 1 as a phospholipid binding machine. Neuron 32, 1057–1069.
Humphrey W, Dalke A, Schulten K (1996). VMD: Visual molecular dynamics. J Mol Graph 14, 33–38.
Jackman SL, Turecek J, Belinsky JE, Regehr WG (2016). The calcium sensor synaptotagmin 7 is required for synaptic facilitation. Nature 529, 88–91.
Jorgensen WL, Chandrasekhar J, Madura JD, Impey RW, Klein ML (1983). Comparison of simple potential functions for simulating liquid water. J Chem Phys 79, 926–935.
Katz AK, Glusker JP, Beebe SA, Bock CW (1996). Calcium ion coordination: a comparison with that of beryllium, magnesium, and zinc. J Am Chem Soc 118, 5752–5763.
Littleton JT, Bai J, Vyas B, Desai R, Baltus AE, Garment MB, Carlson SD, Ganetzky B, Chapman ER (2001). synaptotagmin mutants reveal essential functions for the C2B domain in Ca2+-triggered fusion and recycling of synaptic vesicles in vivo. J Neurosci 21, 1421–1433.
Lynch KL, Gerona RR, Kielar DM, Martens S, McMahon HT, Martin TF (2008). Synaptotagmin-1 utilizes membrane bending and SNARE binding to drive fusion pore expansion. Mol Biol Cell 19, 5093–5103.
MacKerell AD Jr, Bashford D, Bellott M, Dunbrack RL, Evanseck JD, Field MJ, Fischer S, Gao J, Guo H, Ha S, *et al.* (1998). All-atom empirical potential for molecular modeling and dynamics studies of proteins. J Phys Chem B 102, 3586–3616.
Mackerell AD, Feig M, Brooks CL (2004). Extending the treatment of backbone energetics in protein force fields: limitations of gas-phase quantum mechanics in reproducing protein conformational distributions in molecular dynamics simulations. J Comput Chem 25, 1400–1415.
Maximov A, Lao Y, Li H, Chen X, Rizo J, Sorensen JB, Sudhof TC (2008). Genetic analysis of synaptotagmin-7 function in synaptic vesicle exocytosis. Proc Natl Acad Sci USA 105, 3986–3991.
Moghadam PK, Jackson MB (2013). The functional significance of synaptotagmin diversity in neuroendocrine secretion. Front Endocrinol (Lausanne) 4, 124.
Mohrmann R, de Wit H, Connell E, Pinheiro PS, Leese C, Bruns D, Davletov B, Verhage M, Sorensen JB (2013). Synaptotagmin interaction with SNAP-25 governs vesicle docking, priming, and fusion triggering. J Neurosci 33, 14417–14430.
Passmore DR, Rao TC, Peleman AR, Anantharam A (2014). Imaging plasma membrane deformations with pTIRFM. J Vis Exp 2014, 51334.
Phillips JC, Braun R, Wang W, Gumbart J, Tajkhorshid E, Villa E, Chipot C, Skeel RD, Kale L, Schulten K (2005). Scalable molecular dynamics with NAMD. J Comput Chem 26, 1781–1802.
Rao TC, Passmore DR, Peleman AR, Das M, Chapman ER, Anantharam A (2014). Distinct fusion properties of synaptotagmin-1 and synaptotagmin-7 bearing dense core granules. Mol Biol Cell 25, 2416–2427.
Rao TC, Rodriguez ZS, Bradberry MM, Ranski AH, Dahl PJ, Schmidtke MW, Jenkins PM, Axelrod D, Chapman ER, Giovannucci DR, *et al.* (2017). Synaptotagmin isoforms confer distinct activation kinetics and dynamics to chromaffin cell granules. J Gen Physiol 149, 763–780.
Schonn JS, Maximov A, Lao Y, Sudhof TC, Sorensen JB (2008). Synaptotagmin-1 and -7 are functionally overlapping Ca2+ sensors for exocytosis in adrenal chromaffin cells. Proc Natl Acad Sci USA 105, 3998–4003.
Schupp M, Malsam J, Ruiter M, Scheutzow A, Wierda KD, Sollner TH, Sorensen JB (2016). Interactions between SNAP-25 and synaptotagmin-1 are involved in vesicle priming, clamping spontaneous and stimulating evoked neurotransmission. J Neurosci 36, 11865–11880.
Shao X, Fernandez I, Sudhof TC, Rizo J (1998). Solution structures of the Ca2+-free and Ca2+-bound C2A domain of synaptotagmin I: does Ca2+ induce a conformational change? Biochemistry 37, 16106–16115.
Sudhof TC (2013). A molecular machine for neurotransmitter release: synaptotagmin and beyond. Nat Med 19, 1227–1231.
Sudhof TC, Rizo J (1996). Synaptotagmins: C2-domain proteins that regulate membrane traffic. Neuron 17, 379–388.
Sudhof TC, Rothman JE (2009). Membrane fusion: grappling with SNARE and SM proteins. Science 323, 474–477.
Sugita S, Shin OH, Han W, Lao Y, Sudhof TC (2002). Synaptotagmins form a hierarchy of exocytotic Ca(2+) sensors with distinct Ca(2+) affinities. EMBO J 21, 270–280.
Sugita S, Sudhof TC (2000). Specificity of Ca2+-dependent protein interactions mediated by the C2A domains of synaptotagmins. Biochemistry 39, 2940–2949.
Sutton RB, Davletov BA, Berghuis AM, Sudhof TC, Sprang SR (1995). Structure of the first C2 domain of synaptotagmin I: a novel Ca2+/phospholipid-binding fold. Cell 80, 929–938.
Tucker WC, Edwardson JM, Bai J, Kim HJ, Martin TF, Chapman ER (2003). Identification of synaptotagmin effectors via acute inhibition of secretion from cracked PC12 cells. J Cell Biol 162, 199–209.
Voleti R, Tomchick DR, Sudhof TC, Rizo J (2017). Exceptionally tight membrane-binding may explain the key role of the synaptotagmin-7 C2A domain in asynchronous neurotransmitter release. Proc Natl Acad Sci USA 114, E8518–E8527.
Weber JP, Toft-Bertelsen TL, Mohrmann R, Delgado-Martinez I, Sorensen JB (2014). Synaptotagmin-7 is an asynchronous calcium sensor for synaptic transmission in neurons expressing SNAP-23. PLoS One 9, e114033.
Wimley WC, White SH (1996). Experimentally determined hydrophobicity scale for proteins at membrane interfaces. Nat Struct Biol 3, 842–848.
Xue M, Craig TK, Shin OH, Li L, Brautigam CA, Tomchick DR, Sudhof TC, Rosenmund C, Rizo J (2010). Structural and mutational analysis of functional differentiation between synaptotagmins-1 and -7. PLoS One 5.
Zhang X, Rizo J, Sudhof TC (1998). Mechanism of phospholipid binding by the C2A-domain of synaptotagmin I. Biochemistry 37, 12395–12403.
Zhang Z, Hui E, Chapman ER, Jackson MB (2010). Regulation of exocytosis and fusion pores by synaptotagmin-effector interactions. Mol Biol Cell 21, 2821–2831.
Zhang Z, Wu Y, Wang Z, Dunning FM, Rehfuss J, Ramanan D, Chapman ER, Jackson MB (2011). Release mode of large and small dense-core vesicles specified by different synaptotagmin isoforms in PC12 cells. Mol Biol Cell 22, 2324–2336.
Zhou Q, Zhou P, Wang AL, Wu D, Zhao M, Sudhof TC, Brunger AT (2017). The primed SNARE-complexin-synaptotagmin complex for neuronal exocytosis. Nature 548, 420–425.